11^{th} International Conference on Fracture Mechanics of Concrete and Concrete Structures
FraMCoS-11
J. M. Chandra Kishen, A. Ramaswamy, S. Ray and R. Vidyasagar (Eds)
https://doi.org/10.21012/FC11.092375

VIRTUAL EXPERIMENTS FOR STEEL FIBER-REINFORCED HIGH PERFORMANCE CONCRETE BASED ON UNIT CELL CALCULATIONS - NUMERICAL CALIBRATION OF PHENOMENOLOGICAL MATERIAL MODEL

M. PISE*, D. BRANDS*, J. SCHRÖDER*, G. GEBUHR† AND S. ANDERS†

* Institute of Mechanics, Department of Civil Engineering, Faculty of Engineering,
University of Duisburg-Essen, Essen, Germany
e-mail: mangesh.pise@uni-due.de, dominik.brands@uni-due.de, j.schroeder@uni-due.de,

† Chair for Construction Materials, Faculty of Architecture and Civil Engineering,
Bergische Universität Wuppertal, Wuppertal, Germany
e-mail: gebuhr@uni-wuppertal.de, s.anders@uni-wuppertal.de

Key words: Phase-field Model For Fracture, Steel Fiber-Reinforced Concrete, Ellipsoidal Representative Volume Element, Virtual Experiments

Abstract. To facilitate the effective numerical analysis of the fiber-reinforced high performance concrete (HPC) a phenomenological material model is developed. The formulation is derived from the combination of a one-dimensional elasto-plasticity model, which describes the behavior of the embedded fibers in the preferred fiber direction, along with an elasto-plastic phase-field model used to simulate fracture in the HPC matrix. It is essential to take into account the fiber-matrix interactions, microstructure and properties of HPC for the efficient numerical analysis of fiber-reinforced HPC. For this reason, an ellipsoidal unit cell (also known as the representative volume element, RVE) is constructed, which characterizes the behavior of steel fiber-reinforced HPC in the preferred direction of an embedded fiber. The heterogeneity of the real concrete material is taken into account by introducing perturbations to specific material parameters of HPC matrix. In the initial stage of calibration of the presented model, the virtual experiments based on an ellipsoidal RVE are simulated. These simulations are conducted using a micro-mechanical model based on elasto-plastic phase-field model for fracture. Homogenized macroscopic quantities are computed by taking the volume average of corresponding microscopic quantities. In the subsequent stage, macroscopic boundary value problems (BVP) based on a cuboid are simulated on a single scale using the presented phenomenological material model. The efficiency of the presented numerical model is assessed by comparing the simulation results of virtual experiments and macroscopic BVPs using RVEs and cuboids of pure and reinforced HPC, respectively.

1 INTRODUCTION

Fiber-reinforced HPC has recently become a widely popular construction material for structural applications because of its exceptional mechanical properties, e.g., high strength, durability, toughness and ductility, see [1]. Reinforced HPC is a composite material, which is produced by embedding high-strength fibers, e.g. steel fibers, within the concrete matrix. These fibers act as a reinforcement providing better resistance to cracking and improving the load-bearing capacity of concrete under cyclic

loading, see [24]. During the failure process, stresses are transmitted from the concrete matrix to the embedded fibers, effectively restraining further damage in the fiber-reinforced HPC, see [7, 24]. The macroscopic behavior of fiber-reinforced HPC during failure is predominantly governed by the intricate fiber-matrix interactions at the microscale. Therefore, the efficiency of the reinforcement primarily relies on the interaction between the fibers and the surrounding concrete matrix, see [22, 25]. Another significant factor that contributes to exceptional properties of fiber-reinforced HPC is a heterogeneous microstructure, which is characterized by a dense matrix, refined pores and well-distributed reinforcement materials, see [12]. Further research on HPC's behavior at the microstructural level and the significant impact of embedded fibers on the material's overall behavior is essential to enhance the overall performance of fiber-reinforced HPC. Experimental and numerical analysis plays a crucial role in understanding and optimizing the material behavior of fiber-reinforced HPCs before their practical application, especially for reinforced HPCs exposed to cyclic loading. To achieve this objective, the German Research Foundation Priority Programme 2020 (DFG SPP 2020) has been initiated, and the authors of this contribution are collaborating on a joint project focusing on the experimental and numerical analysis of fatigue failure in HPC. Initially, the investigation begins by examining the pullout behavior of a single steel fiber embedded in HPC. This analysis is conducted for the calibration of the micro-mechanical model presented in our recent research works [15,23], which is developed following the phase-field approach for ductile fracture, as introduced in [2, 13]. Therein, the elasto-plastic behavior of concrete is described using the Drucker-Prager plasticity. The material properties of HPC used for the simulations are obtained from experimental measurements, as documented in [5, 11, 19]. In this contribution, the research is focused on the calibration of a macroscopic model, which is based on the superposed models of one-dimensional elasto-plasticity, see [4] and a continuum phase-field model based on the variational formulation of fracture in elasto-plastic material, see [17, 18]. The constitutive framework of a macroscopic model is thoroughly documented in section 2. Virtual experiments based on the constructed ellipsoidal RVE are performed using the micro-mechanical model and the calibrated material parameters for the fiber-pullout test. The homogenized macroscopic quantities are calculated using the procedure outlined in [16, 20]. Macroscopic-BVPs based on the cuboid of pure HPC without perturbation of HPC parameters are simulated for the calibration of the presented numerical model. In section 3, the macroscopic stress-strain characteristics obtained from the simulations of virtual experiments and macroscopic BVPs are compared for the calibration and validation of the presented numerical model. Lastly, the outcomes of the presented work are concluded in Section 5.

2 Constitutive framework

Here, the main idea is the construction of two separate energy functions for the distinct phases in fiber-reinforced HPC, i.e., HPC matrix and embedded steel fibers. The contribution of these energy functions are controlled by the conservation condition $\mathrm{v}^{\mathrm{HPC}} = 1 - \mathrm{v}^{\mathrm{F}}$ using the volume fraction of HPC phase $\mathrm{v}^{\mathrm{HPC}}$ and fiber v^{F}. The additive form of the macroscopic energy function $\bar{\psi}$ is constructed as

$$\begin{aligned}\bar{\psi} = \mathrm{v}^{\mathrm{HPC}}\, \bar{\psi}^{\mathrm{HPC}} \left(\bar{\boldsymbol{\varepsilon}}, \bar{\boldsymbol{\varepsilon}}^{\mathrm{p,HPC}}, \bar{q}, \nabla \bar{q}, \alpha^{\mathrm{HPC}}\right) \\ + \mathrm{v}^{\mathrm{F}}\, \bar{\psi}^{\mathrm{F}} \left(\bar{\boldsymbol{\varepsilon}}, \mathbf{M}, e^{\mathrm{p,F}}, \alpha^{\mathrm{F}}\right) ,\end{aligned} \tag{1}$$

where the total macroscopic strain tensor $\bar{\boldsymbol{\varepsilon}}$ contains the elastic strains $\bar{\boldsymbol{\varepsilon}}^{\mathrm{e,HPC}}$ and the plastic strains $\bar{\boldsymbol{\varepsilon}}^{\mathrm{p,HPC}}$ in HPC phase. An energy function $\bar{\psi}^{\mathrm{HPC}}$ describing the mechanical behavior of HPC phase reads

$$\begin{aligned}\psi^{\mathrm{HPC}} &= g(\bar{q}) \left[\bar{\psi}_0^{\mathrm{e+,HPC}} + \bar{\psi}_0^{\mathrm{p,HPC}} - \psi^{\mathrm{c,HPC}}\right] \\ &+ \bar{\psi}_0^{\mathrm{e-,HPC}} + (1 - g(q))\, \psi^{\mathrm{c,HPC}} \\ &+ \frac{2\,l}{\zeta} \psi^{\mathrm{c,HPC}} \left[\frac{\bar{q}^2}{2l} + \frac{l}{2} \left|\left|\nabla \bar{q}\right|\right|^2\right] ,\end{aligned} \tag{2}$$

where ψ^{c} is the specific critical fracture energy and l is the length scale parameter, cf. [13, 14]. Two different parameters for the critical fracture energy in tension $\psi_{\mathrm{t}}^{\mathrm{c,HPC}}$ and compression $\psi_{\mathrm{c}}^{\mathrm{c,HPC}}$, are considered to capture the distinct behavior of concrete in tension and compression, for details see [23]. Therein, to differentiate the critical fracture energies in tension and compression the sign of the first invariant $\mathrm{tr}\,\bar{\boldsymbol{\sigma}}^{\mathrm{HPC}}$ of the stress tensor for HPC phase is used, cf. [21]. The phase-field parameter $\bar{q} \in [0, 1]$ describes the damage in HPC phase and its gradient is denoted by $\nabla \bar{q}$. A degradation function $g(\bar{q}) = (1 - \bar{q})^m$ is considered. The parameters m and ζ control the degradation characteristics of material during failure, cf. [15, 23]. A reference elastic energy function $\bar{\psi}_0^{\mathrm{e,HPC}}$ associated with the undamaged elastic solid, i.e,

$$\bar{\psi}_0^{\mathrm{e,HPC}} = \frac{\kappa}{2}\mathrm{tr}[\bar{\boldsymbol{\varepsilon}}^{\mathrm{e,HPC}}]^2 + \mu||\mathrm{dev}\,\bar{\boldsymbol{\varepsilon}}^{\mathrm{e,HPC}}||^2\,, \quad (3)$$

is additively decomposed into a positive $\bar{\psi}_0^{\mathrm{e}+}(\bar{\boldsymbol{\varepsilon}}^{\mathrm{e,HPC}})$ and a negative $\bar{\psi}_0^{\mathrm{e}-}(\bar{\boldsymbol{\varepsilon}}^{\mathrm{e,HPC}})$ parts following the split presented in [3]. μ and κ are the Lam*é* coefficients of HPC phase. A plastic energy $\bar{\psi}^{\mathrm{p,HPC}}$ for HPC phase is

$$\bar{\psi}^{\mathrm{p,HPC}}\left(\alpha^{\mathrm{HPC}}\right) = (1-\bar{q})^m\,\bar{\psi}_0^{\mathrm{p,HPC}} \quad \text{with}$$
$$\bar{\psi}_0^{\mathrm{p,HPC}} = y_0^{\mathrm{HPC}}\alpha^{\mathrm{HPC}} + \tfrac{1}{2}\,h^{\mathrm{HPC}}(\alpha^{\mathrm{HPC}})^2\,, (4)$$

where α^{HPC}, y_0^{HPC} and h^{HPC} are the equivalent plastic strain, the yield stress and the hardening parameter for HPC phase, respectively. The energy function $\bar{\psi}^{\mathrm{F}}$ for fiber is constructed using the structural tensor $\mathbf{M} := \boldsymbol{a} \otimes \boldsymbol{a}$, cf. [4], reads

$$\bar{\psi}^{\mathrm{F}} = \bar{\psi}^{\mathrm{e,F}}\left(\bar{\boldsymbol{\varepsilon}}, \mathbf{M}, e^{\mathrm{p,F}}\right) + \bar{\psi}^{\mathrm{p,F}}\left(\alpha^{\mathrm{F}}\right). \quad (5)$$

It characterizes the embedded steel fiber in a preferred fiber direction $\boldsymbol{a}$ with $||\boldsymbol{a}|| = 1$. The total strain tensor e^{F} and the elastic strain tensor $e^{\mathrm{e,F}}$ for fiber can be calculated, respectively as

$$e^{\mathrm{F}} = \bar{\boldsymbol{\varepsilon}} : \mathbf{M} \quad \text{and} \quad e^{\mathrm{e,F}} = e^{\mathrm{F}} - e^{\mathrm{p,F}}\,, \quad (6)$$

where $e^{\mathrm{p,F}}$ denotes a plastic strain tensor for fiber. For the one-dimensional elasto-plasticity problem, an elastic $(\bar{\psi}^{\mathrm{e,F}})$ and a plastic $(\bar{\psi}^{\mathrm{p,F}})$ energy functions are constructed, read

$$\bar{\psi}^{\mathrm{e,F}}\left(\bar{\boldsymbol{\varepsilon}}, \mathbf{M}, e^{\mathrm{p,F}}\right) = \frac{1}{2}\,E^{\mathrm{F}}\left(e^{\mathrm{F}} - e^{\mathrm{p,F}}\right)^2$$
$$\text{and} \quad \bar{\psi}^{\mathrm{p,F}}\left(\alpha^{\mathrm{F}}\right) = y_0^{\mathrm{F}}\,\alpha^{\mathrm{F}} + \frac{1}{2}\,h^{\mathrm{F}}\,(\alpha^{\mathrm{F}})^2\,, \quad (7)$$

where the elastic moduli E^{F}, the equivalent plastic strain α^{F}, initial yield stress y_0^{F} and hardening parameter h^{F} are considered for fiber. The total macroscopic stress tensor $\bar{\boldsymbol{\sigma}}$ is computed by

$$\bar{\boldsymbol{\sigma}} := \mathrm{v}^{\mathrm{HPC}}\,\bar{\boldsymbol{\sigma}}^{\mathrm{HPC}} + \mathrm{v}^{\mathrm{F}}\,\bar{\boldsymbol{\sigma}}^{\mathrm{F}}\,. \quad (8)$$

The stress tensor $\bar{\boldsymbol{\sigma}}^{\mathrm{HPC}}$ for HPC phase and the stress tensor $\bar{\boldsymbol{\sigma}}^{\mathrm{F}}$ for fiber can be derived from the energy functions for the respective phases, i.e., Eq. (2) and Eq. (5), cf. [17, 18]

The system of equations contains, the balance of linear momentum, i.e.,

$$\mathrm{Div}\,\bar{\boldsymbol{\sigma}} = \mathbf{0}\,, \quad (9)$$

and the evolution equation for the phase-field parameter, which reads

$$\bar{q} - l^2\mathrm{Div}(\nabla\bar{q}) - (1-\bar{q})\zeta\mathcal{H}^{\mathrm{HPC}} = 0\,. (10)$$

The value of parameter $m = 2$ is considered to ensure an upper bound of the phase-field $\bar{q} \in [0, 1]$, cf. [9, 14]. Following [13], a local history field function $\mathcal{H}^{\mathrm{HPC}}$ is considered to ensure the irreversibility of the crack evolution as

$$\mathcal{H}^{\mathrm{HPC}} := \max_{s\in[0,t]} \mathcal{H}_0^{\mathrm{HPC}}(\mathbf{x}, \tilde{t}) \geq 0\,, \quad (11)$$

where the maximum value of a dimensionless crack driving state function $\mathcal{H}_0^{\mathrm{HPC}}$ for HPC phase is constructed, i.e.,

$$\mathcal{H}_0^{\mathrm{HPC}} = \left\langle \frac{\mathrm{v}^{\mathrm{HPC}}[\bar{\psi}_0^{\mathrm{e}+,\mathrm{HPC}} + \bar{\psi}_0^{\mathrm{p,HPC}}]}{\psi^{\mathrm{c,HPC}}} - 1 \right\rangle. \quad (12)$$

Two different yield criteria are considered to predict the elasto-plastic behavior of the embedded fibers as well as the concrete. The one-dimensional von Mises yield criterion is used to describe non-linear behavior along the preferred fiber direction, i.e.,

$$\phi^{\mathrm{F}}\left(\bar{\sigma}^{\mathrm{F}}, \kappa_{\mathrm{p}}^{\mathrm{F}}\right) = |\bar{\sigma}^{\mathrm{F}}| - \left(y_0^{\mathrm{F}} + h^{\mathrm{F}}\alpha^{\mathrm{F}}\right)\,, (13)$$

The rate of the plastic strain $\dot{e}^{\mathrm{p,F}}$ and the equivalent plastic strain α^{F} for fiber read

$$\dot{e}^{\mathrm{p,F}} = \lambda^{\mathrm{p,F}} \frac{\partial \phi^{\mathrm{F}}}{\partial \bar{\sigma}^{\mathrm{F}}} \quad \text{and} \quad \dot{\alpha}^{\mathrm{F}} = \lambda^{\mathrm{p,F}} . \tag{14}$$

The associative Drucker-Prager yield criterion is used for HPC phase, which can capture the distinct properties of concrete in tension and compression, i.e.

$$\begin{aligned} \phi^{\mathrm{HPC}} &= \frac{1}{\sqrt{2}} ||\mathrm{dev} \bar{\boldsymbol{\sigma}}_0^{\mathrm{HPC}}|| - \beta_{\mathrm{p}} \mathrm{tr}\, \bar{\boldsymbol{\sigma}}_0^{\mathrm{HPC}} \\ &- \left(y_0^{\mathrm{HPC}} + h^{\mathrm{HPC}} \alpha^{\mathrm{HPC}} \right) , \end{aligned} \tag{15}$$

where β_{p} is a material parameter. The rate of the plastic strains $\dot{\bar{\boldsymbol{\varepsilon}}}^{\mathrm{p,HPC}}$ and the equivalent plastic strains $\dot{\alpha}^{\mathrm{HPC}}$ for HPC phase, i.e.,

$$\dot{\bar{\boldsymbol{\varepsilon}}}^{\mathrm{p,HPC}} = \lambda^{\mathrm{p,HPC}} \frac{\partial \phi^{\mathrm{HPC}}}{\partial \bar{\boldsymbol{\sigma}}_0^{\mathrm{HPC}}}, \ \dot{\alpha}^{\mathrm{HPC}} = \lambda^{\mathrm{p,HPC}} , \tag{16}$$

Here, $\lambda^{\mathrm{p,HPC}}$ denote the incremental plastic consistency parameter for fiber, respectively. For more details about the formulation and implementation of the presented numerical model authors refer to the literature, e.g. [4, 17, 18, 21].

3 Numerical simulations

In this section, the numerical results of virtual experiments and macroscopic BVPs are presented. Simulations for the two types of virtual experiments and macroscopic BVPs, taking into account the homogeneous boundary conditions of the uniaxial tensile tests and the shear tests at the macroscale are conducted. Ellipsoidal RVEs and cuboids of both pure and reinforced HPC are constructed to perform the simulations for virtual experiments and macroscopic BVPs, respectively. To account for the heterogeneity of the real concrete material, the material parameters for the HPC matrix are randomly perturbed. In this study, a 25% perturbation of material parameters, i.e., κ, μ, and ψ^{c}, is considered for both types of simulations. For a comprehensive understanding of the construction procedure for ellipsoidal RVEs and cuboids and the implementation of random perturbation of parameters, refer to [18].

Virtual experiments are performed following a multiscale simulation approach, where an ellipsoidal RVE is attached to the macroscopic material point, e.g., see Fig. 1a and Fig.6a. For these simulations the micro-mechanical model based on the phase-field approach for fracture presented in [15] is used. The material behavior of reinforced HPC along the preferred fiber direction is characterized by the constructed ellipsoidal RVE, as shown in see Fig. 1a and Fig. 6a. This RVE comprises a steel fiber, HPC matrix, and the contact zone between the fiber and matrix. The size of the RVE is selected in such a way that the steel fiber occupies 0.3% of the total volume of the RVE, equivalent to a fiber content of 23 kg/m^3 in the reinforced HPC. Appropriate mechanical and periodic boundary conditions are applied on the ellipsoid RVE at the microscale, for more details on the concepts refer [8, 10]. The ellipsoidal RVE is discretized using 63,232 linear hexahedral elements with exact point symmetry on the lateral surface to apply the periodic boundary conditions.

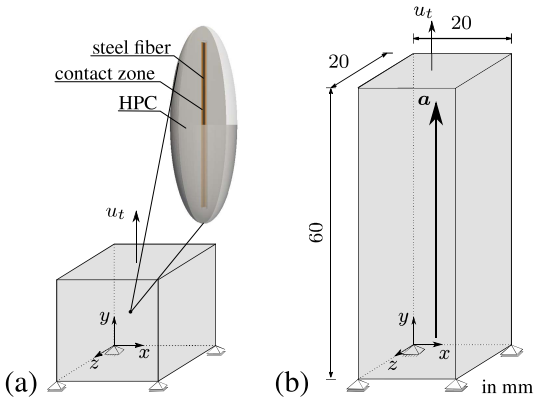

Figure 1: Geometry and boundary conditions for (a) a virtual experiment I with an attached ellipsoidal RVE and (b) a macroscopic BVP I using a cuboid.

A cuboid geometry with homogeneous boundary conditions at macroscale is consider for the simulations of macroscopic BVPs, e.g., see Fig. 1b and Fig. 6b. These simulations are conducted on a single-scale using the presented numerical formulation for macroscopic analysis. The length and width of the cuboid are cho-

sen to be the same as the maximum dimensions of the ellipsoidal RVE, allowing it to accommodate an ellipsoidal RVE within its boundaries. The fibers are oriented with the same preferred direction in the cuboid as in the constructed ellipsoidal RVE, i.e., along the y-axis. The cuboid is discretized for the simulation using 24,000 linear hexahedral elements.

Initially, a virtual experiment I is conducted to simulate a macroscopic homogeneous strain state of a uniaxial tensile test without transverse stresses. Geometry and boundary conditions for a virtual experiment I are shown in Fig. 1a. The experimentally measured mechanical properties of HPC and calibrated material parameters are taken from our recent works [6,18], see Table 1. The computation is carried out by prescribing the value of strain $\bar{\varepsilon}_{22}$ using the macroscopic strain tensor $\bar{\boldsymbol{\varepsilon}}$, i.e.,

$$\bar{\boldsymbol{\varepsilon}} = \begin{bmatrix} \bar{\varepsilon}_{11} & 0 & 0 \\ 0 & \bar{\varepsilon}_{22} & 0 \\ 0 & 0 & \bar{\varepsilon}_{33} \end{bmatrix}. \tag{17}$$

The macroscopic quantities are calculated using the volumetric average of their microscopic counterparts over the RVE, cf. [20] and [16]. The strains $\bar{\varepsilon}_{11}$ and $\bar{\varepsilon}_{22}$ are determinated iteratively to achieve no transverse stresses condition.

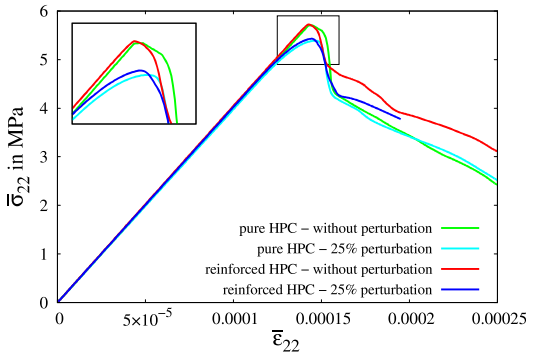

Figure 2: Virtual experiment I: comparison of macroscopic stress-strain characteristic of ellipsoidal RVEs of pure and reinforced HPC without perturbation and with 25% perturbation of HPC parameters.

The macroscopic stress-strain characteristic of ellipsoidal RVEs of pure and reinforced HPC without perturbation and with 25% perturbation of HPC parameters are compared in Fig.2.

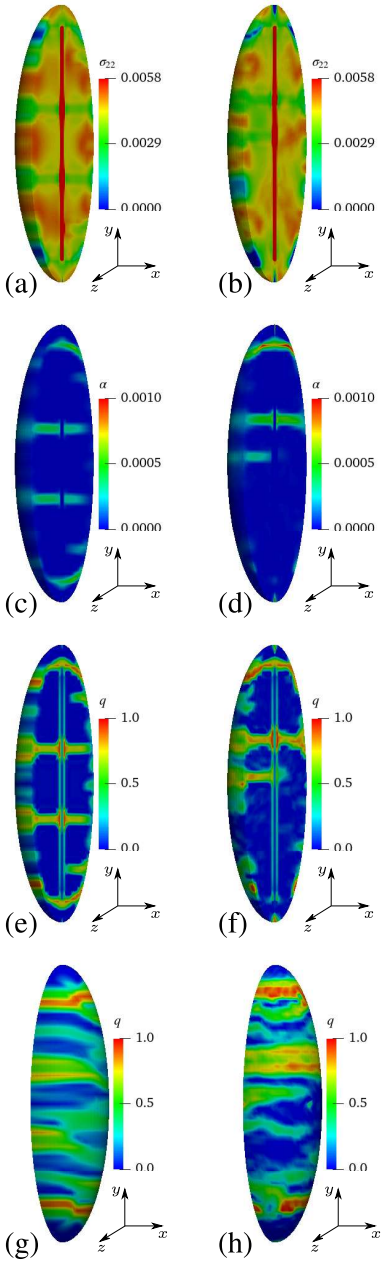

Figure 3: Virtual experiment I - uniaxial tensile test without transverse stresses using ellipsoidal RVEs of reinforced HPC without perturbation (a, c, e, g) and with 25% perturbation of HPC parameters (b, d, f, h): distribution of (a-b) microscopic stresses $\boldsymbol{\sigma}_{22}$ in GPa, (c-d) microscopic equivalent plastic strains α and microscopic phase-field parameter q (e-f) cross-sectional view and (g-h) front view at the macroscopic strain $\bar{\varepsilon}_{22} = 0.000175$.

The microscopic response of ellipsoidal RVEs of reinforced HPC without perturbation, see Fig. 3a,c,e,g and 25% perturbation, see Fig. 3b,d,f,h, are compared.

A macroscopic BVP I considering cuboids of pure and reinforced HPC with homogeneous boundary conditions of a uniaxial tensile test without transverse stresses are simulated using the presented numerical model, Fig. 1b. A volume fraction of $\mathrm{v}^{\mathrm{F}} = 0.003$ is chosen for the cuboid, representing a fiber content of 23 kg/m^3 in the reinforced HPC. The material parameters utilized in the presented phenomenological material model for simulating the macroscopic BVPs are provided in Table 1.

Table 1: Mechanical properties of HPC mixture, calibrated material parameters for HPC phase and material parameters for steel fibers, taken from [6] and [18].

parameter	HPC	unit
E^{HPC}	39.976	GPa
ν^{HPC}	0.192	–
$f_{\mathrm{t}}^{\mathrm{HPC}}$	5.7	MPa
$f_{\mathrm{c}}^{\mathrm{HPC}}$	112	MPa
$\psi_t^{\mathrm{t,HPC}}$	4.2e-4	MPa
$\psi_t^{\mathrm{c,HPC}}$	0.12	MPa
y_0^{HPC}	6.263	MPa
β_{p}	0.5218	–
h^{HPC}	2000	MPa
l	14	mm
m	0.6	–
ζ	0.5	–
parameter	steel fiber	unit
E^{F}	210	GPa
v^{F}	0/0.003	–
y_0^{F}	660	MPa
h^{F}	130	MPa

The same parameter values are used for simulating the macroscopic BVPs for both the HPC phase and the fiber as values used in the virtual experiments, see Table 1. The calibration of parameter l is done by comparing the macroscopic stress-strain curves obtained from the simulations of macroscopic BVP I and virtual experiments I for pure HPC without perturbation. Comparison of the resulting macroscopic stress-strain characteristic for the simulations of virtual experiment I using ellipsoidal RVEs and macroscopic BVP I using cuboids of reinforced HPC without perturbation and with 25% perturbation of HPC parameters are done in Fig. 4a and Fig. 4b, respectively.

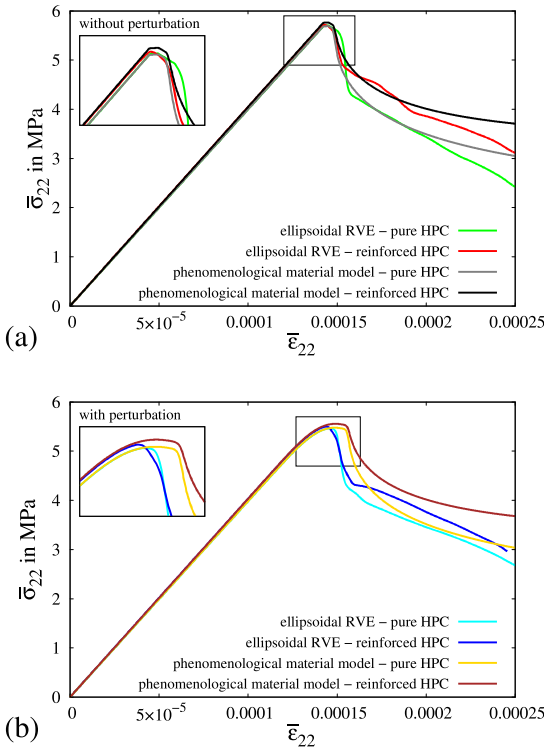

Figure 4: Comparison of macroscopic stress-strain characteristic obtained from the simulation results of virtual experiment I using ellipsoidal RVE and macroscopic BVP I using a cuboid of pure and reinforced HPC, (a) without perturbation and (b) with 25% perturbation of HPC parameters.

The simulation results of macroscopic BVP I with cuboid of reinforced HPC without perturbation, see Figs. 5a,c,e and with 25% pertur-

bation of HPC parameters, see Figs. 5b,d,f are plotted.

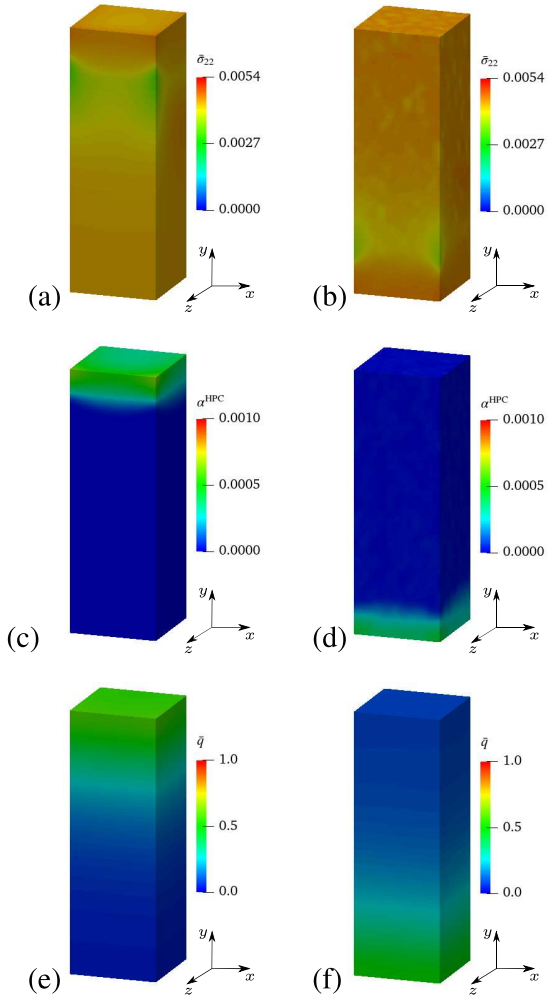

Figure 5: Macroscopic BVP I - uniaxial tensile test without transverse stresses using cuboid of reinforced HPC without perturbation (a, c, e) and with 25% perturbation of HPC parameters (b, d, f): distribution of (b, c) macroscopic stresses $\bar{\sigma}_{22}$ in GPa, (d, e) macroscopic equivalent plastic strains α^{HPC} and (f, g) macroscopic phase-field parameter $\bar{q}$ in HPC phase at the macroscopic strain $\bar{\varepsilon}_{22} = 0.000175$.

Latter, a virtual experiment II is conducted to simulate a macroscopic homogeneous strain state of the shear test. Geometry and boundary conditions for a virtual experiment II are shown in Fig. 6a. The computation is carried out by prescribing the value of strains $\bar{\varepsilon}_{12} = \bar{\varepsilon}_{21}$ using the macroscopic strain tensor $\bar{\varepsilon}$, i.e.,

$$\bar{\varepsilon} = \begin{bmatrix} 0 & \bar{\varepsilon}_{12} & 0 \\ \bar{\varepsilon}_{21} & 0 & 0 \\ 0 & 0 & 0 \end{bmatrix}. \tag{18}$$

The material parameters used for the simulations are same as used in a virtual experiments II, see Table 1.

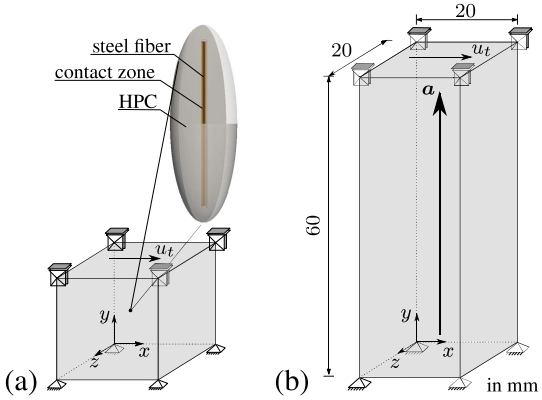

Figure 6: Geometry and boundary conditions for (a) a virtual experiment II with an attached ellipsoidal RVE and (b) a macroscopic BVP II using a cuboid.

In Fig. 7, a comparison is made between the macroscopic stress-strain characteristics, i.e. the volumetric average of microscopic quantities, of ellipsoidal RVEs for pure and reinforced HPC, both without perturbation and with a 25% perturbation of HPC parameters.

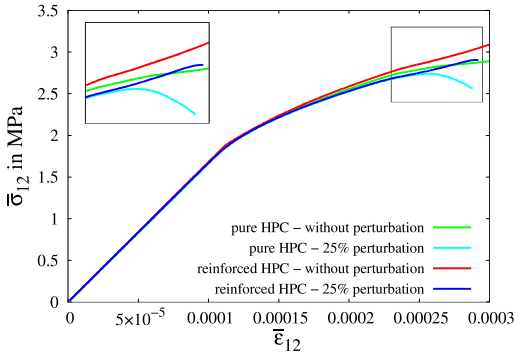

Figure 7: Virtual experiment II: comparison of macroscopic stress-strain characteristic of ellipsoidal RVEs of pure and reinforced HPC without perturbation and with 25% perturbation of HPC parameters.

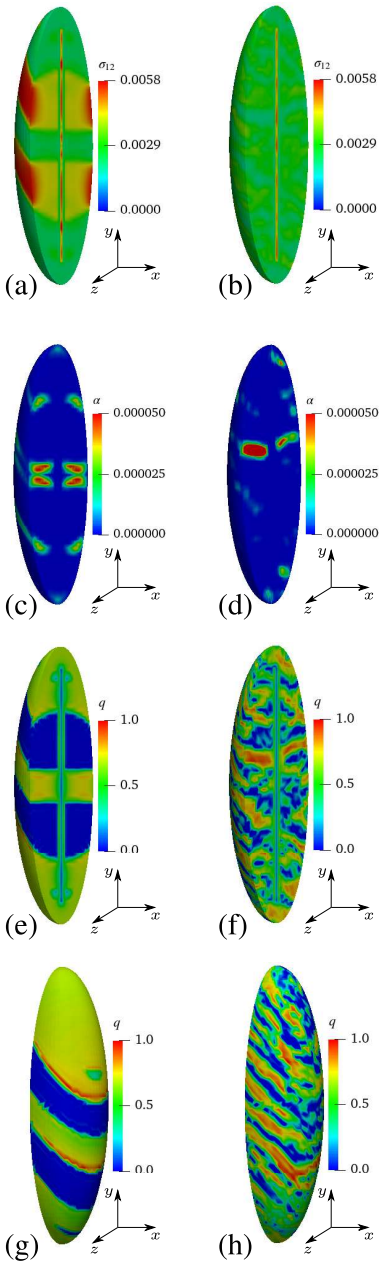

Figure 8: Virtual experiment II - shear test using ellipsoidal RVEs of reinforced HPC without perturbation (a, c, e, g) and with 25% perturbation of HPC parameters (b, d, f, h): distribution of (a-b) microscopic stresses $\boldsymbol{\sigma}_{22}$ in GPa, (c-d) microscopic equivalent plastic strains α and microscopic phase-field parameter q (e-f) cross-sectional view and (g-h) front view at the macroscopic strain $\bar{\varepsilon}_{22} = 0.00025$.

The microscopic response of the ellipsoidal RVEs of reinforced HPC without perturbation, see Fig. 8a,c,e,g and 25% perturbation of HPC parameters, see Fig. 8b,d,f,h, are compared. Comparison of the resulting macroscopic stress-strain characteristic for the simulations of virtual experiment II using ellipsoidal RVEs and macroscopic BVP II using cuboids of reinforced HPC without perturbation and with 25% perturbation of HPC parameters are done in Fig. 9a and Fig. 9b, respectively.

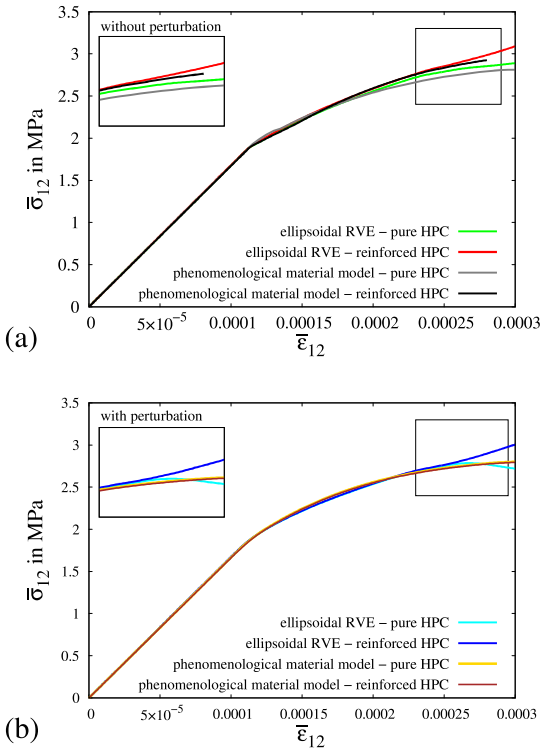

Figure 9: Comparison of macroscopic stress-strain characteristic obtained from the simulation results of virtual experiment II using ellipsoidal RVE and macroscopic BVP II using a cuboid of pure and reinforced HPC, (a) without perturbation and (b) with 25% perturbation of HPC parameters.

The simulation results of macroscopic BVP II with cuboid of reinforced HPC without perturbation, see Figs. 10a,c,e and with 25% perturbation of HPC parameters, see Figs 10b,d,f are plotted.

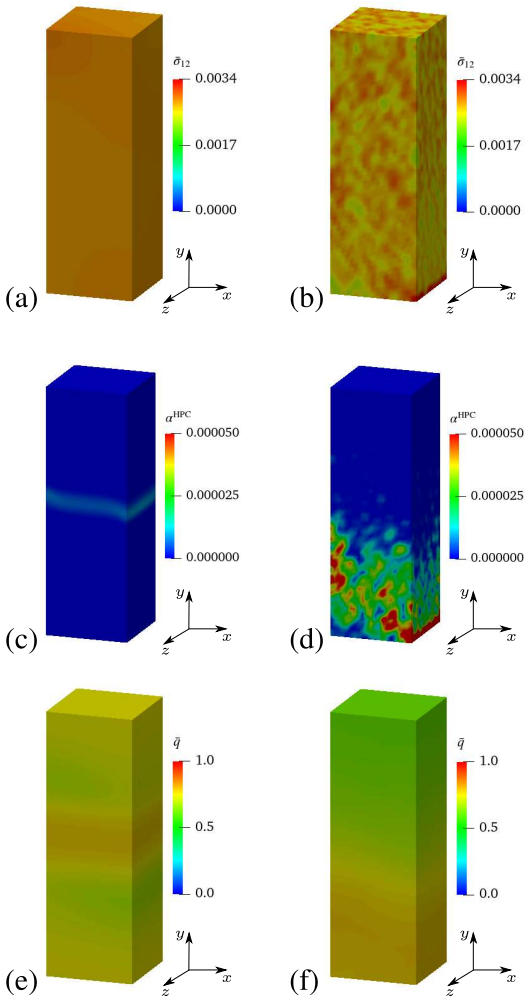

Figure 10: Macroscopic BVP II - shear test using cuboid of reinforced HPC without perturbation (a, c, e) and with 25% perturbation of HPC parameters (b, d, f): distribution of (b, c) macroscopic stresses $\bar{\boldsymbol{\sigma}}_{22}$ in GPa, (d, e) macroscopic equivalent plastic strains α^{HPC} and (f, g) macroscopic phase-field parameter $\bar{q}$ in HPC phase at the macroscopic strain $\bar{\boldsymbol{\varepsilon}}_{22} = 0.00025$.

The comparison of the macroscopic stress-strain plots for the virtual experiments I and II using all four types of RVEs demonstrate the meaningful characteristics, see Figs. 2 and 7. The resulting curves follow initially the same stress-strain characteristic but later they deviate from each other. The macroscopic stress in the reinforced HPC RVEs (blue and red curves) is higher than that in the related pure HPC RVEs (green and cyan curves), see Figs. 2 and 7. Similar characteristics are shown by macroscopic stress-strain curves of RVEs and cuboids of reinforced HPC compared to RVEs and cuboids of pure HPC, see Figs. 4 and 9. In Figs. 2 and 7, the resulting curves for the RVE with perturbation (cyan and blue curves) lie below the resulting curves for the same RVE without perturbation of HPC parameters (green and red curves), respectively. Indeed, this is the desired effect achieved by introducing heterogeneity through random perturbation of parameters. The observation is readily seen when comparing the microscopic responses of RVEs and macroscopic responses of cuboids for both types of tests, with and without considering perturbation. The comparison includes the distribution of stresses, equivalent plastic strain, and phase-field parameter, as shown in Figs. 3, 5, 8, and 10. Nonetheless, the resulting curves for the cuboid of pure and reinforced HPC with perturbation exhibit the higher load-bearing capacity before failure, as compared to the results observed in the ellipsoidal RVEs of pure and reinforced HPC without perturbations, as shown in Fig. 4b. The observed effect is primarily attributed to the random perturbation of critical fracture energies for the concrete matrix. Conversely, in the case of shear tests, the resulting curves for all simulation types exhibit nearly identical behavior initially before diverging at higher strain values, as shown in Figs. 9a,b.

4 Conclusion

The developed phenomenological material model is calibrated, which combines separate energy functions characterizing the behavior of embedded steel fibers and HPC matrix in an additive manner. With this approach, it becomes feasible to simulate the macroscopic behavior of both pure and reinforced HPC using minimal settings. The implementation of various combinations of fiber orientations and distributions can also be achieved effortlessly using this approach. The utilization of different yield criteria for the HPC matrix and fiber makes the presented model effective in capturing the over-

all material behavior of fiber-reinforced HPC, considering the distinct nonlinearities present in each phase. The comparison between the computed macroscopic stress-strain curves from the virtual experiments and the stress-strain characteristics obtained from the simulations of macroscopic BVPs confirms the predictive capabilities of the presented numerical model. However, the macroscopic stress-strain characteristic is notably influenced by the considered heterogeneity introduced through random perturbation of HPC parameters, as observed in the results. This observation can be made by comparing the responses of reinforced HPC with and without perturbation of HPC parameters in the simulation results obtained from both the microscopic-level RVE simulations and macroscopic-level cuboid simulations for both types of tests. As observed, when considering simulations with perturbation of material parameters of HPC, the results obtained using the presented phenomenological material model show marginal differences compared to the results of the virtual experiments. Altogether, the presented model demonstrates efficiency in reproducing similar stress-strain characteristics, especially in the post-critical stress softening region using the calibrated material parameters. Hence, this numerical approach can be further developed to effectively capture the overall material behavior of fiber-reinforced HPC, using the calibrated numerical parameters, and accommodating various fiber distributions and orientations.

Acknowledgement Funded by the Deutsche Forschungsgemeinschaft (DFG, German Research Foundation), Project number: 353513049 (AN1113/2-2, BR5278/2-2, SCHR570/32-2) within the DFG Priority Programme 2020. Computing time provided on the supercomputer magnitUDE, funded by the Deutsche Forschungsgemeinschaft (DFG, German Research Foundation), Project number: 263348352 (INST 20876/209-1 FUGG, INST 20876/243-1 FUGG), is gratefully acknowledged.

REFERENCES

[1] P. C. Aïtcin. *High-performance concrete.* E & FN Spon, London, 1998.

[2] M. Ambati, T. Gerasimov, and L. De Lorenzis. Phase-field modeling of ductile fracture. *Computational Mechanics*, 55(5):1017–1040, 2015.

[3] H. Amor, J. J. Marigo, and C. Maurini. Regularized formulation of the variational brittle fracture with unilateral contact: Numerical experiments. *Journal of the Mechanics and Physics of Solids*, 57:1209–1229, 2009.

[4] J. P. Boehler. *Applications of tensor functions in solid mechanics*, volume 292. Springer, Vienna, 1987.

[5] G. Gebuhr, M. Pise, M. Sarhil, S. Anders, D. Brands, and J. Schröder. Analysis and evaluation of single fibre pull-out behaviour of hooked steel fibres embedded in high performance concrete for calibration of numerical models. *Structural Concrete, Special Issue on Fatigue*, 2019. Submitted.

[6] G. Gebuhr, M. Pise, M. Sarhil, S. Anders, D. Brands, and J. Schröder. Analysis and evaluation of the pull-out behavior of hooked steel fibers embedded in high and ultra-high performance concrete for calibration of numerical models. *Structural Concrete*, 20(4):1254–1264, 2019. 10.1002/suco.201900034.

[7] L. F. Germano, G. Tiberti, and G. Plizzari. Post-peak fatigue performance of steel fiber reinforced concrete under flexure. *Materials and Structures*, 49:4229–4245, 2016.

[8] R. Glüge. Generalized boundary conditions on representative volume elements and their use in determining the effective material properties. *Computational Materials Science*, 79:408–416, 2013.

[9] C. Kuhn, A. Schlüter, and R. Müller. On degradation functions in phase field fracture models. *Computational Materials Science*, 108:374–384, 2015.

[10] F. Larsson, K. Runesson, S. Saroukhani, and R. Vafadari. Computational homogenization based on a weak format of micro-periodicity for RVE-problems. *Computer Methods in Applied Mechanics and Engineering*, 200(1):11–26, 2011.

[11] T. Leusmann, G. Basutkar, and M. Lunardelli. Characterizing the 3d mesostructure of high performance concrete with the help of computed tomography. In I. Gabrijel, C. Grosse, and M. Skazlic, editors, *Proceedings of International Conference on Sustainable Materials, Systems and Structures (SMSS 2019) - Novel Methods for Characterization of Materials and Structures, Rovinj, Croatia*. RILEM, Paris, France, 20-22 March 2019 2019.

[12] P. K. Mehta and P. J. M. Monteiro. *Concrete: microstructure, properties, and materials*. McGraw-Hill, New York, 2014.

[13] C. Miehe, F. Aldakheel, and A. Raina. Phase field modeling of ductile fracture at finite strains: A variational gradient-extended plasticity-damage theory. *International Journal of Plasticity*, 84:1–32, 2016.

[14] C. Miehe, M. Hofacker, and F. Welschinger. A phase field model for rate-independent crack propagation: Robust algorithmic implementation based on operator splits. *Computer Methods in Applied Mechanics and Engineering*, 199:2765–2778, 2010.

[15] M. Pise, D. Brands, M. Sarhil, J. Schröder, G. Gebuhr, and S. Anders. Numerical calibration of elasto-plastic phase-field modeling of fracture for experimental pullout tests of single steel fibres embedded in high-performance concrete. In A. Zingoni, editor, *Advances in Engineering Materials, Structures and Systems: Innovations, Mechanics and Applications: Proceedings of the 7th International Conference on Structural Engineering, Mechanics and Computation (SEMC 2019), Cape Town, South Africa*. Taylor & Francis Group, London, 2019.

[16] M. Pise, D. Brands, J. Schröder, G. Gebuhr, and S. Anders. On the application of representative volume elements for steel fiber reinforced high performance concrete - a numerical study. *Proceedings in Applied Mathematics and Mechanics*, 20(1):e202000323, 2020.

[17] M. Pise, D. Brands, J. Schröder, G. Gebuhr, and S. Anders. Macroscopic model for steel fiber reinforced high performance concrete based on unit cell calculations. *Proceedings in Applied Mathematics and Mechanics*, 21(1):e202100180, 2021.

[18] M. Pise, D. Brands, J. Schröder, G. Gebuhr, and S. Anders. Macroscopic model based on application of representative volume element for steel fiber reinforced high performance concrete. In A. Zingoni, editor, *Current Perspectives and New Directions in Mechanics, Modelling and Design of Structural Systems: Proceedings of the Eigth International Conference on Structural Engineering, Mechanics and Computation (SEMC 2022), Cape Town, South Africa*, pages 1300–1306. CRC Press, Oxon, United Kingdom, 2022.

[19] T. Scheiden and N. Oneschkow. Influence of coarse aggregate type on the damage mechanism in high-strength concrete under compressive fatigue loading. *Structural Concrete*, 20:1212–1219, 2019.

[20] J. Schröder. A numerical two-scale homogenization scheme: the FE^2-method. In

J. Schröder and K. Hackl, editors, *Plasticity and Beyond - Microstructures, Crystal-Plasticity and PhaseTransitions*, volume 550, chapter ,CISM Lectures Notes, pages 1–64. Springer, Vienna, 2014.

[21] J. Schröder, M. Pise, D. Brands, G. Gebuhr, and S. Anders. Phase-field modeling of fracture in high performance concrete during low-cycle fatigue: numerical calibration and experimental validation. *Computer methods in applied mechanics and engineering*, 398:115181, 2022. doi.org/10.3390/ma15031179.

[22] A. Sivakumar and M. Santhanam. Mechanical properties of high strength concrete reinforced with metallic and non-metallic fibres. *Cement and Concrete Composites*, 29(8):603–608, 2007.

[23] J. Storm, M. Pise, D. Brands, J. Schröder, and M. Kaliske. A comparative study of micro-mechanical models for fiber pullout behavior of reinforced high performance concrete. *Engineering Fracture Mechanics*, 243:107506, 2021. 10.1016/j.engfracmech.2020.107506.

[24] J. Zhang. *Fatigue Fracture of Fibre Reinforced Concrete*. PhD thesis, Technische Universität von Dänemark, 1998.

[25] G. Žirgulis, O. Švec, E. V. Sarmiento, M. R. Geiker, A. Cwirzen, and T. Kanstad. Importance of quantification of steel fibre orientation for residual flexural tensile strength in FRC. *Materials and Structures*, 49(9):3861–3877, 2016.